Mapping gradient-driven morphological phase transition at the conductive domain walls of strained multiferroic films

M. J. Han,[1,2] E. A. Eliseev,[3] A. N. Morozovska,[4,*] Y. L. Zhu,[1] Y. L. Tang,[1] Y. J. Wang,[1] X. W. Guo,[1,5] and X. L. Ma[1,6,†]

[1]*Shenyang National Laboratory for Materials Science, Institute of Metal Research, Chinese Academy of Sciences, Wenhua Road 72, 110016 Shenyang, China*

[2]*University of Chinese Academy of Sciences, Yuquan Road 19, 100049 Beijing, China*

[3]*Institute for Problems of Materials Science, National Academy of Sciences of Ukraine, Krjijanovskogo 3, 03142 Kyiv, Ukraine*

[4]*Institute of Physics, National Academy of Sciences of Ukraine, 46, Prospekt Nauky, 03028 Kyiv, Ukraine*

[5]*University of Science and Technology of China, Jinzhai Road 96, 230026 Hefei, China*

[6]*State Key Lab of Advanced Processing and Recycling on Non-ferrous Metals, Lanzhou University of Technology, Langongping Road 287, 730050 Lanzhou, China*

(Received 22 April 2019; revised manuscript received 15 August 2019; published 11 September 2019)

The coupling between antiferrodistortion (AFD) and ferroelectric (FE) polarization, universal for all tilted perovskite multiferroics, is known to strongly correlate with domain wall functionalities in the materials. The intrinsic mechanisms of domain wall phenomena, especially AFD-FE coupling-induced phenomena at the domain walls, have continued to intrigue the scientific and technological communities because of the need to develop future nanoscale electronic devices. Over the past years, theoretical studies have often shown controversial results, owing to the fact that they are neither sufficiently nor directly corroborated with experimental evidence. In this work, the AFD-FE coupling at uncharged 180° and 71° domain walls in $BiFeO_3$ films is investigated by means of aberration-corrected scanning transmission electron microscopy with high-resolution scanning transmission electron microscopy and rationalized by phenomenological Landau-Ginzburg-Devonshire (LGD) theory. We reveal a peculiar morphology at the AFD-FE walls, including kinks, meandering, and trianglelike regions with opposite oxygen displacements and curvature near the interface. The LGD theory confirms that the tilt gradient energy induces these unusual morphologies and the features would change delicately with different kinds of domain walls. Moreover, the 180° AFD-FE walls are proved to be conductive with an unexpected reduction of the Fe-O-Fe bond angle, which is distinct from theoretical predictions. By exploring AFD-FE coupling at the domain walls, and its induced functionalities, we provide exciting evidence into the links between structural distortions and its electronic properties, which provide great benefit for fundamental understanding of domain wall functionalities as well as functional manipulations for novel nanodevices.

DOI: 10.1103/PhysRevB.100.104109

I. INTRODUCTION

Multiferroics, with simultaneous coexistence of ferroic long-range orders and accompanying unusual physical properties, are regarded as fertile systems for condensed matter physics and multifunctionalities. As a result, exploring the interplay among these order parameters of different nature, such as ferroelectric (FE) polarization, antiferrodistortive (AFD), ferromagnetic (FM), or antiferromagnetic (AFM) orders has been regarded as a key issue both for fundamental studies and future applications [1–3]. Meanwhile, domain walls, due to their recently discovered manifold unusual physical properties, offer us an excellent platform for the corresponding investigations [4–6].

Domain walls are reported to perform series novel functionalities, including large local conductivity [4], photovoltaic effect [7,8], magnetoelectric response [9,10] and even superconductivity [11], which confirm that the wall itself can act as an active element in functional devices. Except for the exciting functionalities, the hidden physical mechanisms underlying the domain walls' responsibility for the interacting and competing lattice, charge, spin, and orbital degrees of freedom still require fundamental investigations [12,13]. Surprisingly, all these physical mechanisms and properties can be traced to the changes of the fundamental unit in transition metal oxides with an ABO_3 perovskite structure—the BO_6 octahedra. The arrangements or symmetry of the corner-sharing octahedral network in perovskites are reported to be strongly coupled with the electronic, magnetic, and optical properties [14,15]. Investigations on the AFD characteristics and the coupling of AFD, FE, and FM order parameters at domain walls would help us better understand the structure of the walls, permitting the explanation of wall multiferroicity in terms of their underlying structure and make it more accessible to control the specific functionalities. For instance, Catalan *et al.* [16,17] reported that the local conduction may be generated by the considerably reduced electronic band gap that corresponds to the straightening of the octahedral rotation at the domain walls using first-principles calculations. Besides, first-principles calculations also show that the changes in the

*anna.n.morozovska@gmail.com
†xlma@imr.ac.cn

Fe-O-Fe bond angles in $BiFeO_3$ (BFO) at the domain walls may change the canting of the Fe magnetic moments accordingly, and end up with enhanced local magnetization at the domain walls [18]. Moreover, the interplay between strain, FE, AFE, and AFD long-range order parameters would generate a lot of remarkable functionalities, including flexoelectric, rotostriction, and flexoantiferrodistortive effects through calculations [19–22].

Compared to the abundant theoretical results reported on FE and AFD coupling at domain walls, experimental studies of the coupling are quite rare. Previous experimental studies on domain walls are mostly focused on the FE nature of the domain walls. The AFD characteristics, especially the AFD-FE coupling at the domain walls, are rarely addressed. One reason is that it is still a challenge to probe both the AFD and FE characteristics locally at the domain walls, though the local probing is urgent for understanding of the AFD-FE interplay. Possible causes may be the large lattice and octahedra distortions at the domain walls which make it harder to probe the FE and AFD characteristics at the atomic scale. Except for this, the out-of-phase rotation of oxygen octahedra in BFO, the only multiferroics reported at room temperature [23] makes it rather difficult to detect the rotation angle along the $[100]_{pc}$ direction. Borisevich *et al.* [24] reported an atomically abrupt octahedral tilt transition across charged domain walls compared with a diffuse associated polarization profile through principle component analysis based on simultaneously acquired high-angle annular dark-field (HAADF) and annular bright-field (ABF) images. However, the coupling between FE and AFD at domain walls and its influence on the local properties are far from being settled.

In this work, we used high-resolution scanning transmission electron microscopy (HRSTEM) to acquire HAADF and ABF images at the 180° and 71° domain walls in BFO films and extract the FE polarization and AFD characteristics locally around the domain walls directly from the ion positions in the images. Unusual AFD-FE wall morphologies including kinks, meandering, and trianglelike regions with opposite oxygen displacements and curvature near the interface, are observed. Landau-Ginzburg-Devonshire (LGD) theory based calculations confirm that the meandering domain walls originate from the tilts gradient energy in thin BFO films, whereas the curvature near the interface at 71° domain walls is induced by the surface influence. Most importantly, we observed an obvious conductivity accompanied with a distinct decrease of Fe-O-Fe bond angle around in-plane axis at 180° domain walls, which is completely different from previous reports. Thus, we provide direct experimental evidences for AFD-FE coupling and put forward that the correlated conduction may be ascribed to the reduction of Fe-O-Fe bond angle at 180° domain walls, which may enlighten the study on corresponding electronic properties.

II. RESULTS

A. Material preparation and experimental methods

We used pulsed laser deposition (PLD) to grow 7- and 18-nm BFO films on $PrScO_3$ (PSO; $a = 5.608$ Å; $b = 5.780$ Å; $c = 8.025$ Å) $(001)_O$ (subscript "O" denotes the orthorhombic orientation) substrates. The laser we used is a Coherent ComPex PRO 201 F KrF ($\lambda = 248$ nm) excimer laser. The target we used is a sintered stoichiometric BFO ceramic 1 in. in diameter. Commercial, one-side polished PSO $(001)_O$ oriented substrates with dimensions of 10 mm × 10 mm × 0.5 mm were used for film deposition. All of the substrates were heated up to 850 °C for 20 min before deposition to clean the surface. The target-substrate distance was set at 32 mm. During the deposition, the substrate temperature was set at 800 °C, the oxygen pressure was set at 12 Pa, the repetition rate was set at 6 Hz, and the laser energy applied was 2 J cm^{-2}. After deposition, the samples were kept at 800 °C for 5 min and then cooled down to room temperature at 5 K min^{-1} in an oxygen pressure of 3×10^4 Pa.

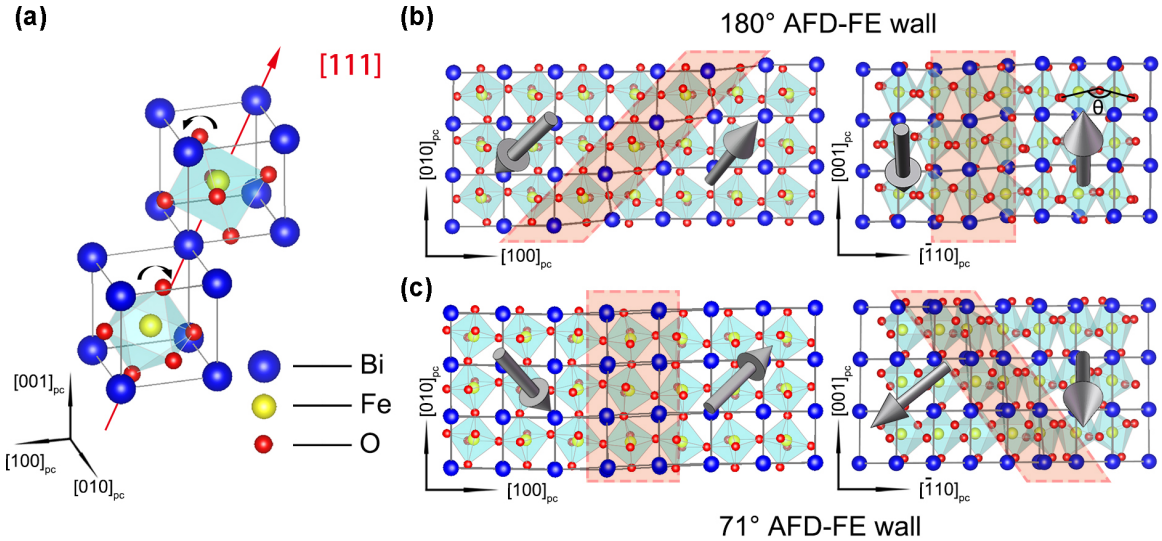

FIG. 1. Crystal structures showing the AFD-FE walls in BFO film. (a) Atomic structure of bulk BFO crystal showing the oxygen octahedral rotation (black curved arrows). (b), (c) Atomic structure models for 180° (b) and 71° (c) AFD-FE walls projected along $[001]_{pc}$ and $[110]_{pc}$ directions.

A traditional method (slicing, gluing, grinding, dimpling, and ion milling) is used to prepare the specimens for HAADF-STEM imaging. For the final ion milling we used a Gatan 691 PIPS at a voltage lower than 1 kV to reduce the ion beam damage. A Titan Cubed 60–300 kV microscope (FEI) was used to acquire the atomic resolved HAADF and ABF images. The aberration-corrected scanning transmission electron microscope is fitted with a monochromator, a high-brightness field-emission gun (X-FEG) and double aberration (Cs) correctors operating at 300 kV. The semiconvergence angle is set at 21.4 mrad. To carry out the atom column positions, we used MATLAB software to fit them as two-dimensional (2D) Gaussian peaks [25–27].

The local piezoresponse was carried out by PFM on a commercial AFM system (Cypher, Asylum Research) in ambient conditions at room temperature. The contact frequency for VPFM measurements is set around 350 kHz. The conductive AFM (CAFM) was carried out by the same system with an Orca holder using Ti/Ir (5/20) coated tips (ASYELEC-01-R) with nominal $k = 2.8\,\mathrm{N\,m^{-1}}$. To perform CAFM on the cross-sectional sample, a thin graphite layer was deposited on the back side of the specimen.

B. Experimental results for AFD-FE walls

The AFD order parameter corresponds to the rotations of oxygen octahedra as shown in Fig. 1(a). The deformation or rotation of the oxygen octahedra can give rise to new functionalities. Particularly, ferroelectric domain walls would generate changes in polarization and oxygen octahedra at the same time. The coupling between them ends up with different AFD-FE walls in ferroelectric films [see Figs. (1b) and 1(c)]. To demonstrate the AFD and FE coupling at the domain walls, we study the 180° and 71° walls in BFO films with different thicknesses grown on PSO $(001)_O$ substrates (see Fig. S1 in the Supplemental Material [28]). Since the oxygen octahedra in BFO share an out-of-phase rotation along the $[100]_{pc}$ direction, in order to demonstrate the AFD walls and FE walls at the same time, we managed to acquire the HAADF and ABF images for cross-sectional BFO films projecting along the $[110]_{pc}$ direction.

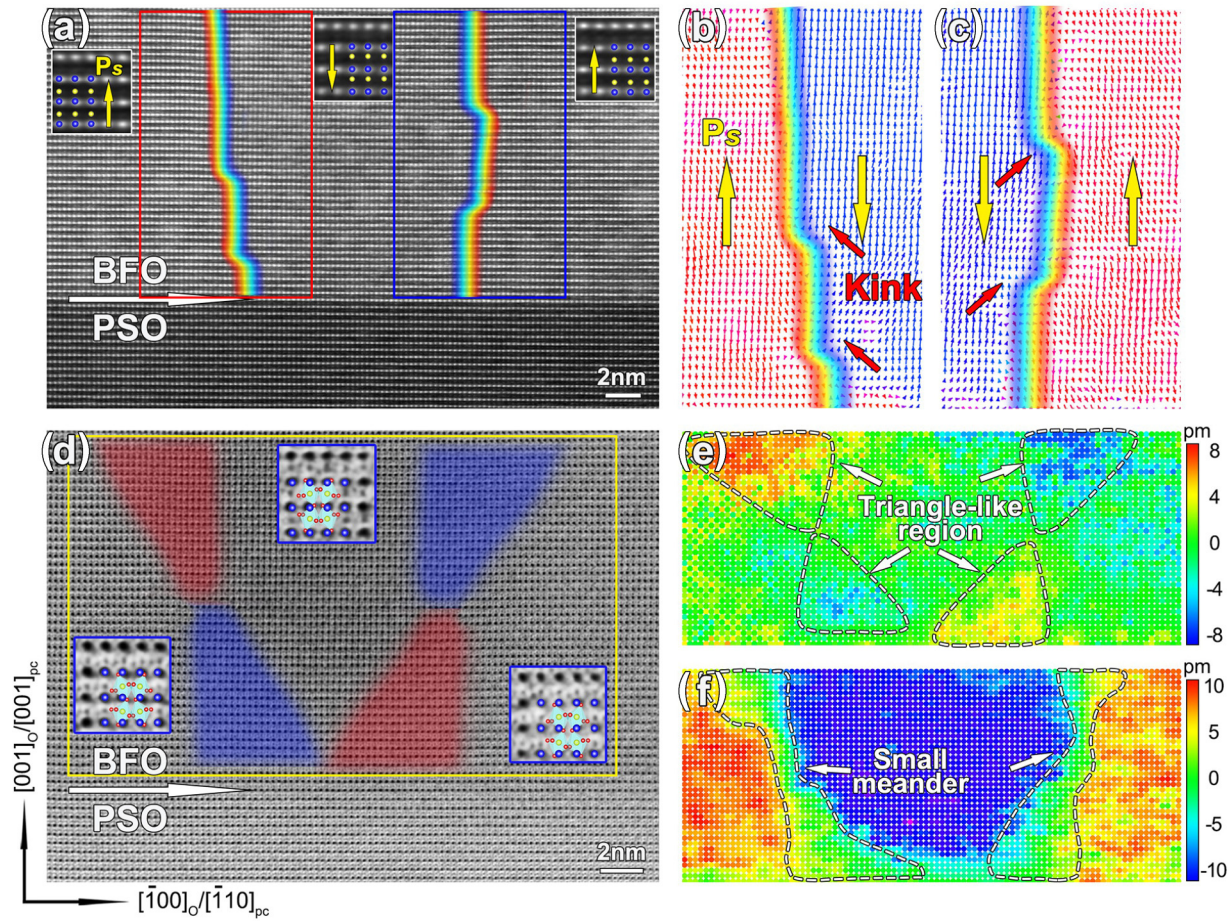

FIG. 2. An 18-nm BFO film grown on PSO $(001)_O$ substrate (180° domain wall). (a) Cross-sectional HAADF image of BFO/PSO interface project along the $[110]_{pc}$ direction. Two 180° domain walls are marked. The insets are enlarged images of each domain. The blue and yellow solid circles denote the position of Bi^{3+} and Fe^{3+} columns. The yellow arrows denote the polarization direction in each domain. (b), (c) are Fe^{3+} displacements mapping of the red and blue rectangles in (a), respectively. The kinked domain walls are marked by red arrows. (d) ABF image of the same area as panel (a). The red and blue trianglelike regions are marked to demonstrate the AFD walls. The blue insets are superposition of the atomic schematics with enlarged images of each domain. Images (e), (f) are oxygen displacement components along $[\bar{1}10]_{pc}$ and $[001]_{pc}$, respectively. The trianglelike regions and AFD wall meandering are marked by white dotted areas.

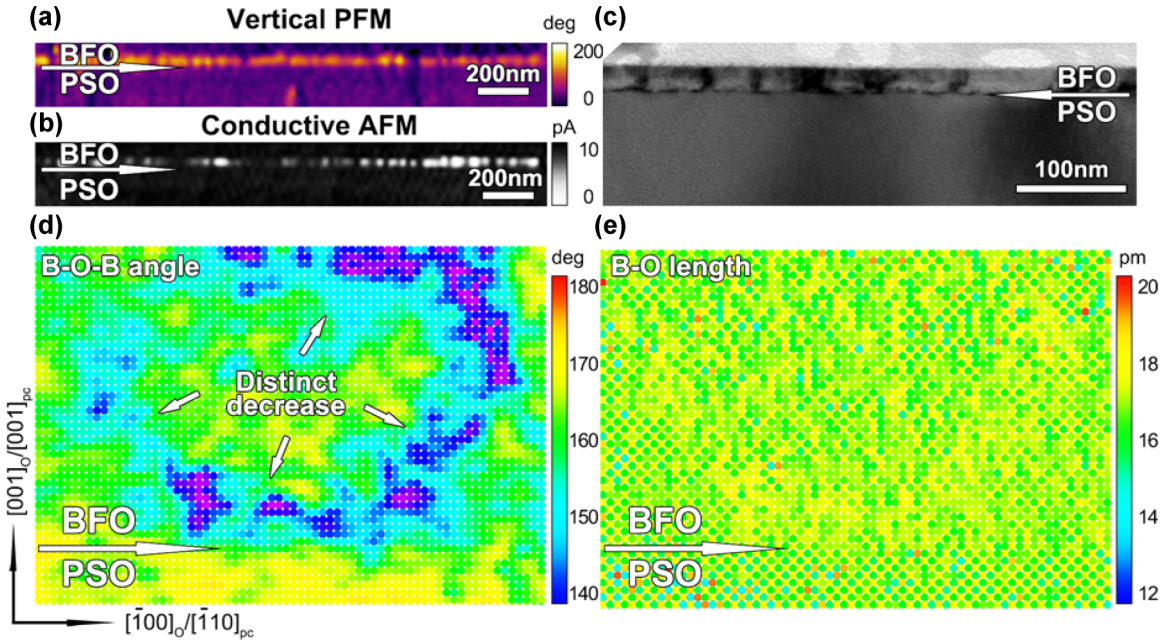

FIG. 3. Conductive AFM and corresponding *B*-O-*B* bond analyses for 18-nm BFO film grown on PSO $(001)_O$ substrate with 180° domain walls. (a), (b) Vertical PFM (a) and corresponding conductive AFM (b) images for 180° domain walls. (c) TEM bright-field image for BFO film. (d), (e) *B*-O-*B* bond angle (d) and *B*-O bond length (e) distributions corresponding to the 180° domain walls in Fig. 2.

The $(\bar{1}10)$ oriented 180° domain walls in an 18-nm BFO film grown on PSO substrate are shown in Fig. 2. The cross-sectional HAADF image of BFO film [see Fig. 2(a)] reveals two 180° domain walls in it. The enlarged images, which reveal clear opposite Fe^{3+} ion displacements, are shown as the inset in each domain. The polarization directions (opposite to the Fe^{3+} ion displacements) are also marked by the yellow arrows in Fig. 2(a). Detailed analyses on the 180° domain walls in the red and blue rectangles are shown in Figs. 2(b) and 2(c), respectively. The 180° FE domain walls are quite straight except for several kinks (marked by the red arrows). Compared to this, the 180° AFD walls are much more tortuous based on the oxygen octahedra displacements extracted from ABF images of the domain walls [see Fig. 2(d)]. Despite the opposite polarization directions, all of the domains demonstrate a checkerboard pattern of oxygen displacements, which can be clearly seen in the insets in Fig. 2(d). Figures 2(e) and 2(f) are oxygen displacements along in-plane and out-of-plane directions, respectively, which reveal a significant discrepancy between the FE and AFD walls. Particularly, there exist two trianglelike regions with opposite oxygen displacements (the red and blue areas marked by white dashed lines) at each domain wall in Fig. 2(e). It seems that the different oxygen displacement regions are related to the polarization direction in the two domains. The slightly smaller oxygen displacements at the interface compared to the ones at the surface are supposed to come from the large tensile strain from the substrate. Besides this, the oxygen displacements along the out-of-plane direction demonstrate a significant meandering of the AFD walls [marked by the white dashed areas in Fig. 2(f)]. There also exist small meandering areas at each domain wall, which are marked by the white arrows in Fig. 2(f).

We perform *in situ* piezoresponse force microscopy (PFM) and conductive atomic force microscopy (CAFM) measurements on the cross-sectional TEM samples to probe electronic properties of the domain walls (see typical example in Fig. 3). The stripelike contrast in the BFO layer in Fig. 3(a) (vertical PFM response) corresponds to the 180° domains in BFO film which agree well with the TEM bright-field image in Fig. 3(c). Although with limited space resolution in AFM, the 180° domain walls still demonstrate a significant conductivity [CAFM response is shown in Fig. 3(b)]. Note that the PFM and CAFM maps are all acquired around the [110] axis which corresponds to exactly the cross-sectional lamellae examined in the TEM. It is reported that the high conductivity can be related with the strengthening (increasing) of the Fe-O-Fe bond angle, which would give rise to a reduced electronic band gap at the domain walls [16,17]. However, the strengthening of the Fe-O-Fe bond angle has not been proved from our experiments. In contrast to this, the $[110]_{pc}$ projected Fe-O-Fe bond angles [the angle θ in Fig. 1(b)] shown in Fig. 3(d), which were deduced from the O and Fe ion column positions in Fig. 2(d), reveal a distinct decrease. Meanwhile, the $[110]_{pc}$ projected *B*-O bond length does not show any obvious changes at the 180° domain walls [see Fig. 3(e)]. Since the changes in oxygen octahedral tilt angle would influence the orbital overlap and change the electronic band gap [16,17] in the film, we tend to believe it is the reduction of the *B*-O-*B* bond angle caused by the AFD-FE coupling that gives rise to the conduction at the domain walls.

The 71° domain walls in 7-nm BFO film grown on the PSO substrate are also analyzed for further investigation of AFD-FE coupling at the domain walls (see Fig. 4). The polarization directions (opposite to the Fe^{3+} ion displacements) marked by the yellows arrows in Fig. 4(a) demonstrate a clear

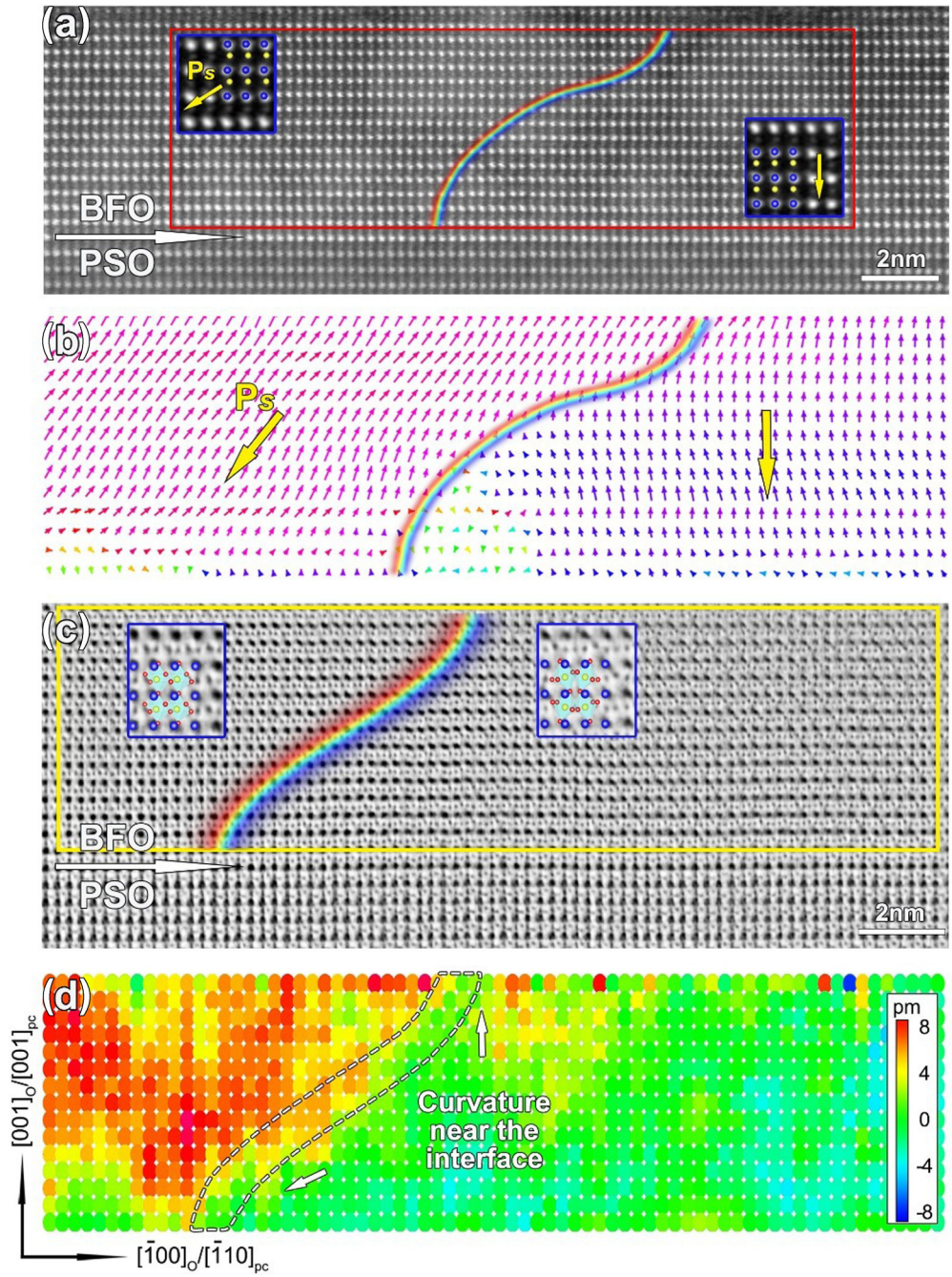

FIG. 4. A 7-nm BFO film grown on PSO $(001)_O$ substrate (71° domain wall). (a) HAADF image of BFO/PSO interface. The 71° domain wall is marked. The insets are enlarged images of each domain. The blue and yellow solid circles denote the position of Bi^{3+} and Fe^{3+} columns. The blue arrows denote the polarization direction in each domain. (b) Fe^{3+} displacements mapping of the red rectangle in panel (a). (c) ABF image of the 71° domain wall. The 71° AFD wall is marked. The blue insets are superpositions of the schematics with enlarged images of each domain. (d) Oxygen displacement components along the $[\bar{1}10]_{pc}$ direction. The AFD wall broadenings are marked by white dotted areas. The white arrows denote the curvature near the interfaces.

71° domain wall. A detailed analysis on the 71° domain walls inside the red rectangle is shown in Fig. 4(b). It can be seen that the 71° FE domain walls bend at the interface and the surface, as distinct from the 180° domain walls. The ABF image of the 71° domain wall [shown in Fig. 4(c)] demonstrates the coexistence of uniform spatial distribution (left) and a checkerboard pattern (right) of oxygen displacements. Figure 4(d) shows oxygen displacements along the in-plane direction, which demonstrate the increased width of the AFD wall compared to the FE wall and significant curvature at the interface and surface [marked by the white arrows in Fig. 4(d)].

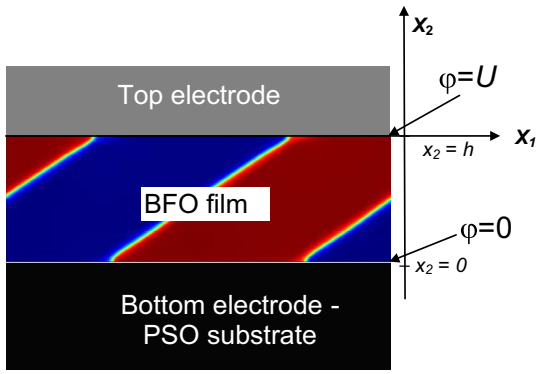

FIG. 5. Considered system for modeling. Considered system, consisting of thin BFO film, placed between electrically conducting top and bottom electrodes, and PSO substrate. The {111} cut with domain stripes is shown.

C. Model and parameters for theoretical description

Schematics of the considered system, consisting of a thin BFO film, namely, its {111}-cut with incline domain stripes, placed between electrically conducting top and bottom electrodes, and PSO substrate are shown in Fig. 5. The considered nominally uncharged 180° and 71° domain walls (DWs) in BFO are shown in Figs. 1(b) and 1(c). To simplify the consideration of 71° DWs we changed the coordinate frame from pseudocubic to orthorhombic settings by the rotation around the X_2 axis on the $\pi/4$ angle. The two-dimensional (2D) problem was solved numerically by finite element modeling (FEM). Initial distributions of tilt and polarization components were taken in the form of 180° or 71° straight domain structures superimposed on the random distribution with a very small amplitude.

We use a phenomenological LGD theory to model the domain walls (DWs) morphology in a thin BFO film placed on a thick PSO substrate. Two vectorial order parameters, namely, polarization components P_i and oxygen octahedral tilts Φ_i, are used for the description of the FE and AFD components of the DWs ($i = 1, 2, 3$). The bulk part of the LGD thermodynamic potential consists of the following contributions:

$$G_V = \int_S dx_1 dx_3 \int_0^h (\Delta G_{\text{AFD}} + \Delta G_{\text{FE}} + \Delta G_{\text{BQC}} + \Delta G_{\text{striction}} + \Delta G_{\text{elast}} + \Delta G_{\text{flexo}}) dx_2. \quad (1)$$

In Eq. (1) all contributions are consistent with the parent phase $m3m$ symmetry in accordance with the basics of the LGD approach. The compact form of the AFD contribution is

$$\Delta G_{\text{AFD}} = b_i(T)\Phi_i^2 + b_{ij}\Phi_i^2\Phi_j^2 + b_{ijk}\Phi_i^2\Phi_j^2\Phi_k^2 + v_{ijkl}\frac{\partial\Phi_i}{\partial x_k}\frac{\partial\Phi_j}{\partial x_l}. \quad (2a)$$

In accordance with the classical Landau approach, we assume that the coefficients b_i are temperature dependent. In accordance with experiments [29], the dependence can be described by a Barrett law [30], $b_i = b_T T_{q\Phi}[\coth(T_{q\Phi}/T) - \coth(T_{q\Phi}/T_\Phi)]$, where T_Φ is the AFD transition temperature and $T_{q\Phi}$ is a characteristic temperature. Description and numerical values of the phenomenological coefficients b_i, b_{ij}, and b_{ijk}, and gradient coefficients v_{ij} included in Eq. (2a) can be found in Table I, where Voigt notations are used.

The compact form of the FE contribution is

$$\Delta G_{\text{FE}} = a_i(T)P_i^2 + a_{ij}P_i^2P_j^2 + a_{ijk}P_i^2P_j^2P_k^2 + g_{ijkl}\frac{\partial P_i}{\partial x_k}\frac{\partial P_j}{\partial x_l} - P_iE_i. \quad (2b)$$

In accordance with the LGD approach that is well adopted for proper and incipient ferroelectrics, the coefficients a_k are temperature dependent and obey the Barrett law, $a_k^{(P)} = \alpha_T[T_{qP}\coth(T_{qP}/T) - T_C]$, where T_C is the Curie temperature and T_{qP} is a characteristic temperature [21,29,30]. The full form of Eqs. (1) and (2) is listed in Appendix A in the Supplemental Material [28].

Description and numerical values of the phenomenological coefficients a_i, a_{ij}, and a_{ijk}, and gradient coefficients g_{ij} included in Eq. (2b) can be found in Table I. Electric field components E_i are defined via electrostatic potential in the conventional way, $E_i = -\partial\varphi/\partial x_i$. The potential satisfies the Poisson equation, $\varepsilon_0\varepsilon_{\text{eff}}\frac{\partial^2\varphi}{\partial x_i^2} = \frac{\partial P_i}{\partial x_i}$, where the effective dielectric permittivity, $\varepsilon_{\text{eff}} = \sum_i \varepsilon_{bi} + \varepsilon_{el}$, includes a background permittivity [31], Jahn-Teller modes, and electronic contributions, which in total can be pretty high for BFO. Electric boundary conditions for the short-circuited film are the zero electric potential at the conducting electrodes, $\varphi|_{x_2=0,h} = 0$.

The compact form of the biquadratic coupling energy between polarization and tilt is

$$\Delta G_{\text{BQC}} = \xi_{ijkl}\Phi_i\Phi_jP_kP_l, \quad (2c)$$

As one can see, the coupling energy (2c) includes poorly known tensorial AFD-FE biquadratic coupling coefficients ξ_{44}, ξ_{11}, and ξ_{12}, which have been treated as fitting parameters to experiment (listed in Table I).

Electrostriction and rotostriction contributions are

$$\Delta G_{\text{striction}} = -Q_{ijkl}\sigma_{ij}P_kP_l - R_{ijkl}\sigma_{ij}\Phi_k\Phi_l. \quad (2d)$$

Electrostriction and rotostriction coefficients, Q_{ijkl} and R_{ijkl}, are listed in Table I. Elastic and flexoelectric energies are

$$\Delta G_{\text{elast}} = -s_{ijkl}\sigma_{ij}\sigma_{kl} - \frac{F_{ijkl}}{2}\left(\sigma_{ij}\frac{\partial P_k}{\partial x_l} - P_k\frac{\partial\sigma_{ij}}{\partial x_l}\right). \quad (2e)$$

Here s_{ijkl} are the components of the elastic compliance tensor (see, e.g., Ref. [32]) and F_{ijkl} are flexoelectric tensor components (listed in Table I).

Note that we could not find the gradient coefficients, g_{ij} and v_{ij}, as well as flexoelectric tensor components, F_{ij}, for BFO in the literature and therefore treated them as fitting parameters. We vary them in typical ranges established for other tilted perovskites [37]. The concrete values of g_{ij} and v_{ij} listed in Table I were fitted to reproduce correctly the width of experimentally observed DWs. It appeared that FEM results are very sensitive to g_{ij} and v_{ij}, and less sensitive to F_{ij}, until they are significantly smaller than the critical values, estimated for the $m3m$ parent phase by Yudin *et al.* [38]. With increase of F_{ij} above the critical values, that is, about 5.75×10^{-11} m^3/C, the spatially modulated phase may

TABLE I. Parameters used in LGD calculations for AFD-FE perovskite BFO.

Parameter	Designation	Numerical values for BFO	Reference
Effective permittivity	$\varepsilon_{\text{eff}} = \Sigma_i \varepsilon_{bi} + \varepsilon_{el}$	160	Fitting parameter
Dielectric stiffness	$\alpha_T (\times 10^5\ \text{C}^{-2}\,\text{J m/K})$	9	[a]
Curie temperature for P	T_C(K)	1300	[a]
Barrett temperature for P	T_{qP}(K)	800	[a]
Coefficients at P^4	$a_{ij} (\times 10^8\ \text{C}^{-4}\,\text{m}^5\,\text{J})$	$a_{11} = -13.5$, $a_{12} = 5$	[a]
Coefficients at P^6	$a_{ijk} (\times 10^9\ \text{C}^{-6}\,\text{m}^9\,\text{J})$	$a_{111} = 11.2$, $a_{112} = -3$, $a_{123} = -6$	[a]
Electrostriction coefficients	Q_{ij} ($\text{C}^{-2}\,\text{m}^4$)	$Q_{11} = 0.054$, $Q_{12} = -0.015$, $Q_{44} = 0.02$	[b]
Elastic stiffness	$c_{ij} (\times 10^{11}$ Pa)	$c_{11} = 3.02$, $c_{12} = 1.62$, $c_{44} = 0.68$	[c]
Polarization gradient coefficients	$g_{ij} (\times 10^{-10}\ \text{C}^{-2}\,\text{m}^3\,\text{J})$	$g_{11} = 10$, $g_{12} = -7$, $g_{44} = 5$	Fitting parameter
AFD-FE coupling coefficients	$\xi_{ij} (\times 10^{29}\ \text{C}^{-2}\,\text{m}^{-2}\,\text{J/K})$	$\xi_{11} = -0.5$, $\xi_{12} = 0.5$, $\xi_{44} = -2.6$	[a,d]
Coefficients at Φ^2	$b_T [\times 10^{26} \cdot \text{J}/(\text{m}^5\,\text{K})]$	4	[a]
Curie temperature for Φ	T_Φ(K)	1440	[a]
Barrett temperature for Φ	$T_{q\Phi}$(K)	400	[a]
Coefficients at Φ^4	$b_{ij} (\times 10^{48}\ \text{J/m}^7)$	$b_{11} = -24 + 4.5[\coth(300/T) - \coth(3/14)]$ $b_{12} = 45 - 4.5(\coth(300/T) - \coth(1/4))$	[a]
Coefficients at Φ^6	$b_{ijk} (\times 10^{70}\ \text{J/m}^9)$	$b_{111} = 4.5 - 3.4[\coth(400/T) - \coth(2/7)]$ $b_{112} = 3.6 - 0.04[\coth(10/T) - \coth(1/130)]$ $b_{123} = 41 - 43.2[\coth(1200/T) - \coth(12/11)]$	[a]
Tilt gradient coefficients	$n_{ij} (\times 10^{11}\ \text{J/m}^3)$	$\nu_{11} = 2$, $\nu_{12} = -1$, $\nu_{44} = 1$	Fitting parameter
Rotostriction coefficients	$R_{ij} (\times 10^{18}\ \text{m}^{-2})$	$R_{11} = -1.32$, $R_{12} = -0.43$, $R_{44} = 8.45$	[b]
Flexoelectric tensor components	$F_{ij} (\times 10^{-11}\ \text{m}^3/\text{C})$	$F_{11} = 2$, $F_{12} = 1$, $F_{44} = 0.5$	Fitting parameter
Flexocoupling/flexovoltage coefficients	f_{ij}(V)	$f_{11} = 9.3$, $f_{12} = 7.9$, $f_{44} = 0.34$	Fitting parameter

[a]Karpinsky *et al.* [33].
[b]Morozovska *et al.* [34].
[c]Zhang *et al.* [35].
[d]Eliseev *et al.* [36].

appear firstly at domain walls and then propagate the film entirely with further increase of F_{ij}.

The surface energy of the film has the following form:

$$\int_S \left(\frac{b_i^{(S)}}{2} \Phi_i^2 + \frac{a_i^{(S)}}{2} P_i^2 \right) dx_1 dx_3. \tag{3}$$

Surface energy coefficients $b_i^{(S)}$ and $a_i^{(S)}$ have a different nature and control the broadening at the surface of ADF and FE domain walls, respectively.

The coupled system of Euler-Lagrange equations allowing for Khalatnikov relaxation of the oxygen tilt and polarization components Φ_i and P_i is

$$\frac{\delta G}{\delta P_i} = -\Gamma \frac{\partial P_i}{\partial t} \quad \text{and} \quad \frac{\delta G}{\delta \Phi_i} = -\Gamma \frac{\partial \Phi_i}{\partial t}. \tag{4a}$$

These equations are supplemented by the boundary conditions of zero generalized fluxes at the film boundaries,

$$b_i^{(S)} \Phi_i + v_{ijkl} \frac{\partial \Phi_j}{\partial x_k} n_l \Big|_{x_2=0,h} = 0,$$

$$a_i^{(S)} P_i + g_{ijkl} \frac{\partial P_j}{\partial x_k} n_l \Big|_{x_2=0,h} = 0, \tag{4b}$$

without summation on $i = 1, 2, 3$ and n_l are the components of external normal to the film surfaces $x_2 = 0, h$. The explicit form of Eq. (4) is listed in Appendix B of the Supplemental Material [28]. The natural boundary conditions used hereinafter correspond to the case $b_i^{(S)} = 0$ and $a_i^{(S)} = 0$.

Elastic problem formulation is based on the equations of state, $u_{ij} = -\frac{\delta G}{\delta \sigma_{kl}}$, where u_{ij} are elastic strain tensor components. Mechanical equilibrium conditions are $\partial \sigma_{ij}/\partial x_j = 0$ [30].

The misfit strain u_m appears from the difference between the lattice constants of the film and substrate [39], and so we suppose that the misfit strain $u_{11} = u_{33} = u_m$ is applied into the XZ plane at the BFO-PSO interface $x_2 = 0$. In order to estimate the misfit strain for BFO film on orthorhombic PSO substrates at room temperature (RT), we used a pseudocubic lattice constant obtained as the cubic root of the elementary cell volume (see Table II). Note that the misfit strain u_m contributes to the elastic boundary conditions:

$$\sigma_{ij} n_j|_{x_2=h} = 0, \quad (U_1 - u_m x_1)|_{x_2=0} = 0,$$
$$U_2|_{x_2=0} = 0, \quad (U_3 - u_m x_3)|_{x_2=0} = 0. \tag{5}$$

D. Modeling of polarization and tilt behavior in a thin BFO film on $PrScO_3$ substrate

The problem described above [see Eqs. (1)–(5)] was analyzed numerically using FEM for a 5–20-nm-thick BFO film

TABLE II. Parameters used for misfit strain estimation in BFO thin films on PSO substrate.

Parameter description	Numerical value
Lattice constants of $PrScO_3$ at RT (Å)	$a = 5.608$; $b = 5.780$; $c = 8.025$
Pseudocubic "lattice constant" (Å)	4.021[a]
BFO film thickness h (nm)	18 nm, 7 nm
BFO pseudocubic lattice constant (Å)	$3.9916 + 6.9 \times 10^{-5}(T - 295)$[b]
Misfit strain u_m (%) at RT	1.8%

[a]See Gesing *et al.* [40].
[b]The dependence was extrapolated to room temperature from higher temperature using the data of Ref. [34].

on PSO substrate. The morphology of nominally uncharged DWs in thin BFO film is shown in Figs. 6–8. The film orientation with respect to substrate was {101} and {110}, respectively. Different orientations of DWs are considered below, namely, 180° and 71° walls, schematics of which are shown in Figs. 1(b) and 1(c). The values of the gradient coefficients chosen for Figs. 6–8 correspond to the maximal qualitative similarity with experimental results for all films.

Unusual morphologies of the 180° DW structure in an epitaxial {101}-oriented 18-nm BFO film grown on PSO substrate are presented in Fig. 6. Curved DWs appeared to be long-living (meta)stable distributions of polarization and tilt, which have been relaxed at times $t \gg \tau_K$ from the initial ($t = 0$) straight orientation of the DW at room temperature. It is seen that all components of tilt change sign across the incline AFD-FE domain wall. Two trianglelike regions with opposite orientation of the tilt component Φ_1 across curved 180° DWs are presented in Fig. 6(a) at $t = 13\tau_K$. The relaxed curved and meandering profiles of Φ_2 are shown in Fig. 6(b) at $t = 13\tau_K$ and $26\tau_K$. Noticeably curved and "zigzaglike" meandering Φ_3 distribution are shown in Fig. 6(c) at $t = 13\tau_K$. The tilt walls can meander freely because the AFD component of the DW is not affected by any sort of "deelastification" field.

At the same time the polarization components P_1 and P_2 are affected by depolarization electric field (produced by $\mathrm{div}\vec{P} \neq 0$), but its influence significantly decreases with $\varepsilon_{\mathrm{eff}}$ increase above 100. At $\varepsilon_{\mathrm{eff}} \geqslant 100$, P_1 is almost zero everywhere, but reveals clearly visibly thin meandering regions at the walls [see Fig. 6(d)]. The profiles of P_2 across 180° DWs reveal noticeable meandering superimposed on a trianglelike motif [see Fig. 6(e)]. The relative straightening of $P_{1,2}$ walls happens only at $\varepsilon_{\mathrm{eff}} \approx \varepsilon_b \leqslant 10$, because the system tries to minimize the high energy of the electric depolarization film that is produced by any sort of charged DWs [31,36,41], and the only way to do this is to keep $P_1 \approx 0$ and P_2 walls relatively straight. The distribution $P_3(x_1, x_2)$ is not affected by the depolarization field. Therefore the meandering of P_3 walls, which originates from the biquadratic AFD-FE coupling and surface influence via the natural boundary conditions, correlates with meandering $\Phi_{2,3}$ walls [compare Fig. 6(f) with Figs. 6(b) and 6(c)].

The features of meandering morphologies of the 180° DW structure "survive" in a {101}-oriented 18-nm BFO film even after a very long relaxation time (see Fig. 7). Specifically, curved and meandering DWs appeared thermodynamically stable at room temperature. Several curved regions with nonzero Φ_1 of the opposite orientation, small and evolved meanders at domain walls of Φ_2 and Φ_3, are seen in Figs. 7(a)–7(c). The profiles of polarization components P_1, P_2, and P_3 correlate with the meandering of Φ_2 and Φ_3 walls, but the depolarization keeps P_2 walls more straight. Note that the left and right parts of Fig. 7 refer to the distributions of different physical quantities, namely, the left color maps are the rotation angle of oxygen octahedra [Figs. 7(a)–7(c)] and the right ones are polarization components [Figs. 7(d)–7(f)] across the AFD-FE domain wall. Since the gradient coefficients of $\mathbf{P}$ and $\mathbf{\Phi}$ are different (see Table I), the characteristic length scale that determines the transverse and longitudinal scales of the transition region at the wall are also different. As a result, the length scale of the wall meandering appears to be more than the film thickness (18 nm). The situation looks like the random seeding (superimposed on a straight wall) evolves into a meander for the right wall (four curved features), while the left wall demonstrates only one curved feature. To simulate the meandering of both (left and right) walls thicker films should be considered. Actually, additional calculations proved that left and right walls contain approximately equal amounts of meanders for a film thickness of more than 40 nm. However, the concrete position of the meanders along the wall does depend on the random seeding. This is similar to the so-called sampling (or realization) effect we revealed earlier [42] for labyrinthine domains in spherical ferroelectric nanoparticles, where different random seedings evolve into different curved, meandering, kinks, or/and labyrinthine domains. However, the domain morphology, such as characteristic sizes of the curved walls, remains the same. This means that the meandering is not merely an inherent property of the wall, but rather a manifestation of the tilts and polarization gradient instability [36] evolving from random fluctuations (modeled by random initial conditions).

The question about the appearance of the meandering instability of the AFD-FE domain walls in BFO films was studied in detail in Ref. [36]. It was shown without consideration of misfit effect, electrostrictive, and rotostriction coupling [36], and confirmed in this work with these effects included, that the origin of the meandering 180° AFD-FE walls in thin BFO films is conditioned by the decrease of the tilt gradient energy. We checked numerically that the origin of the meandering walls does not stem from incomplete polarization screening in thin BFO films, electrostrictive, rotostrictive, or flexoelectric coupling. The spatial confinement delineates the appropriate boundary conditions for the oxygen tilt and

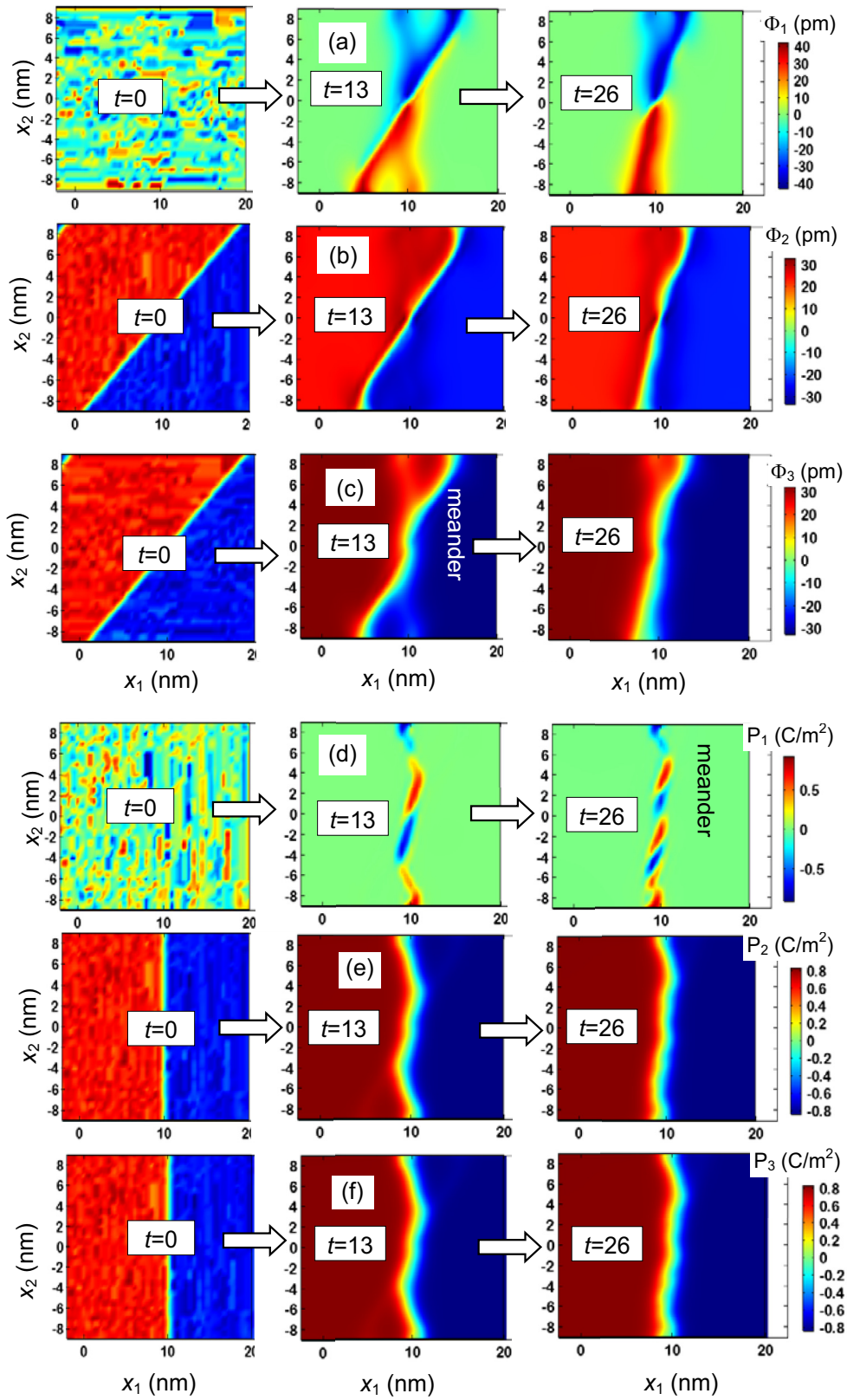

FIG. 6. {101} oriented 180° DWs in 18-nm BFO film on $PrScO_3$ substrate, relaxing from initial straight DWs at $t = 0$ to the intermediate state $t = 13\tau_K$, and than to the final state $t > 25\tau_K$. Distribution of the AFD order parameter Φ_i (a)–(c) and polarization P_i (d)–(f) components in the cross section of a thin BFO film with {101} oriented 180° DWs. Film thickness is 18 nm, room temperature. Tilted coordinate system is used for x_1.

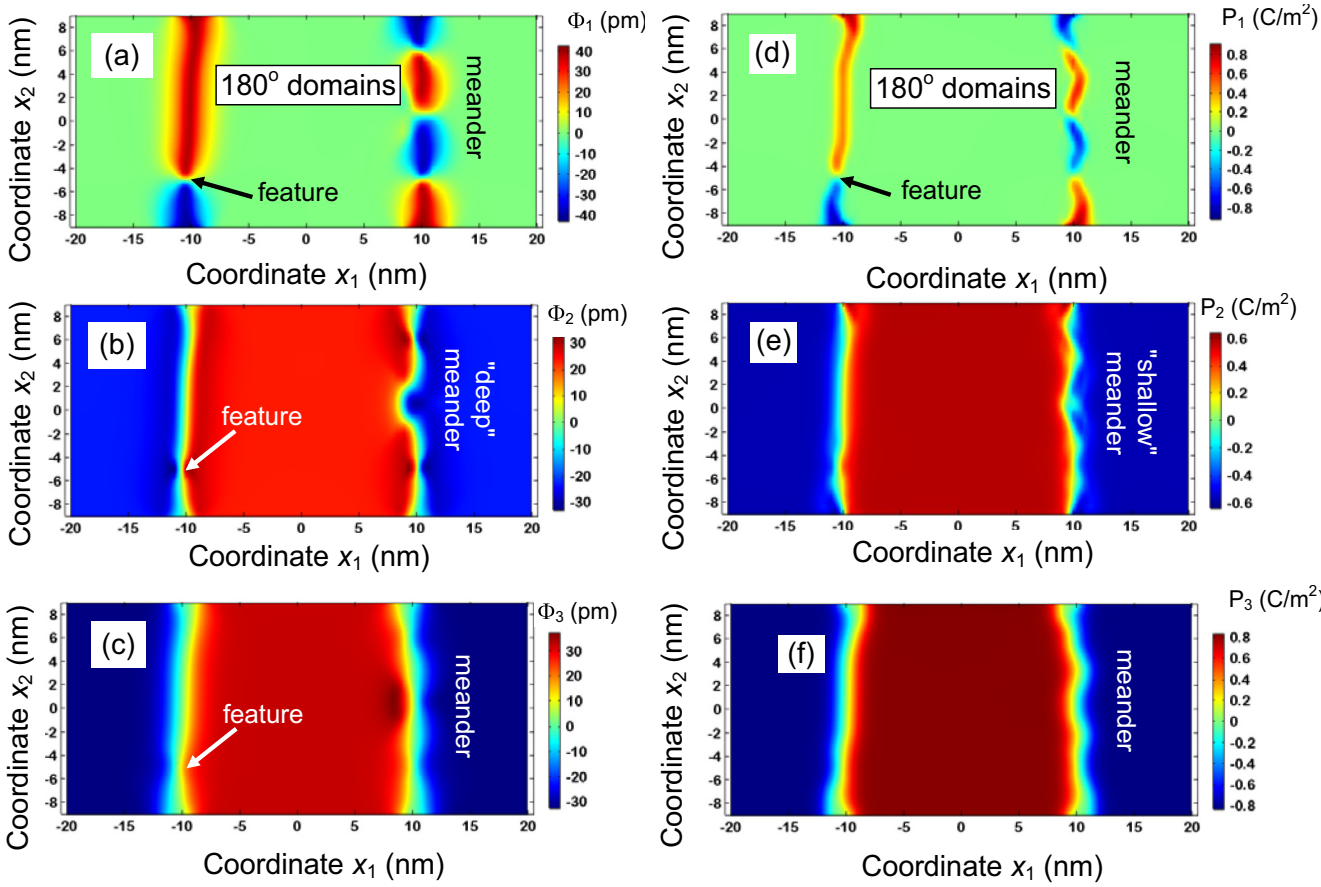

FIG. 7. {101} oriented 180° DWs in 18-nm BFO film on $PrScO_3$ substrate, after a very long relaxation time. Distribution of the AFD order parameter Φ_i (a)–(c) and polarization P_i (d)–(f) components in the $\{x_1x_2\}$ cross section of a thin BFO film with {101} oriented 180° DWs. Film thickness is 18 nm, room temperature. Tilted coordinate system is used for x_1.

polarization components at the film surfaces, but its existence is not critical for the appearance of meandering walls and their zigzag stability. The values of the gradient energy coefficients for the oxygen tilt appeared critical to initiate the morphological changes of the 180° uncharged domain walls towards zigzag meandering. Meandering instability appears for small gradient energies, while the walls become straighter and broaden at higher gradients.

Currently we can add to the knowledge that a "meandering" state occurs near the 180° AFD-FE domain walls, for which the symmetry determined by the ratio between the different components of the order parameters differs from the symmetry far from the walls. However, such a "quasidomain" of the new phase creates strong internal fields (elastic and electric ones) and, as a result, it itself breaks up into secondary domains. Since the quasidomain is localized near the wall separating the classical ("primary") domains, the combination of primary and secondary domains gives a meandering wall.

Typical morphologies of the 71° DW structure in epitaxial {110}-oriented 7-nm BFO film grown on PSO substrate are shown in Fig. 8. Bulk 71° domains correspond to the case when only one component of the vectorial order parameter changes its sign when crossing the wall plane. For the case when DWs are inclined and curved near the electrodes for all components of polarization and tilt, no meandering instability or zigzag changes appear in the case, but the DW width increases with the tilt gradient coefficient increase. The inclination of the 71° DW is determined by the conditions of electrical and mechanical compatibility, while the bending of the DW near the film surfaces is induced by the surface influence. That is, since we used the natural boundary conditions, it means that the corresponding gradients of order parameters are zero at the surface, and hence the DWs should be perpendicular to the surface at the surface, while it is inclined in the central part of the film.

In accordance with theoretical estimates (see Appendix E in the Supplemental Material [28]), the experimentally observed conductivity enhancement at the domain wall can be caused by the electric potential and elastic strain variations inside the wall [43]. The electroelastic potential relief (wells or humps) leads to higher concentration of electrons (or holes) in the DW due to the local band bending. It appeared that the contribution of the strain variations to the conductivity modulation is dominant, because the potential is zero exactly at the 180° and 71° DWs. Since the strain variation is proportional to $Q_{ijkl}P_kP_l + R_{ijkl}\Phi_k\Phi_l + F_{ijkl}\frac{\partial P_k}{\partial x_l}$, it may also include the atomic bond changes at the wall via the striction and flexoelectric mechanisms. It should be noted that within the LGD model any structural change (e.g., via octahedral tilting coupled with rotostriction mechanism, $\delta u_{ij} \cong R_{ijkl}\Phi_k\Phi_l$)

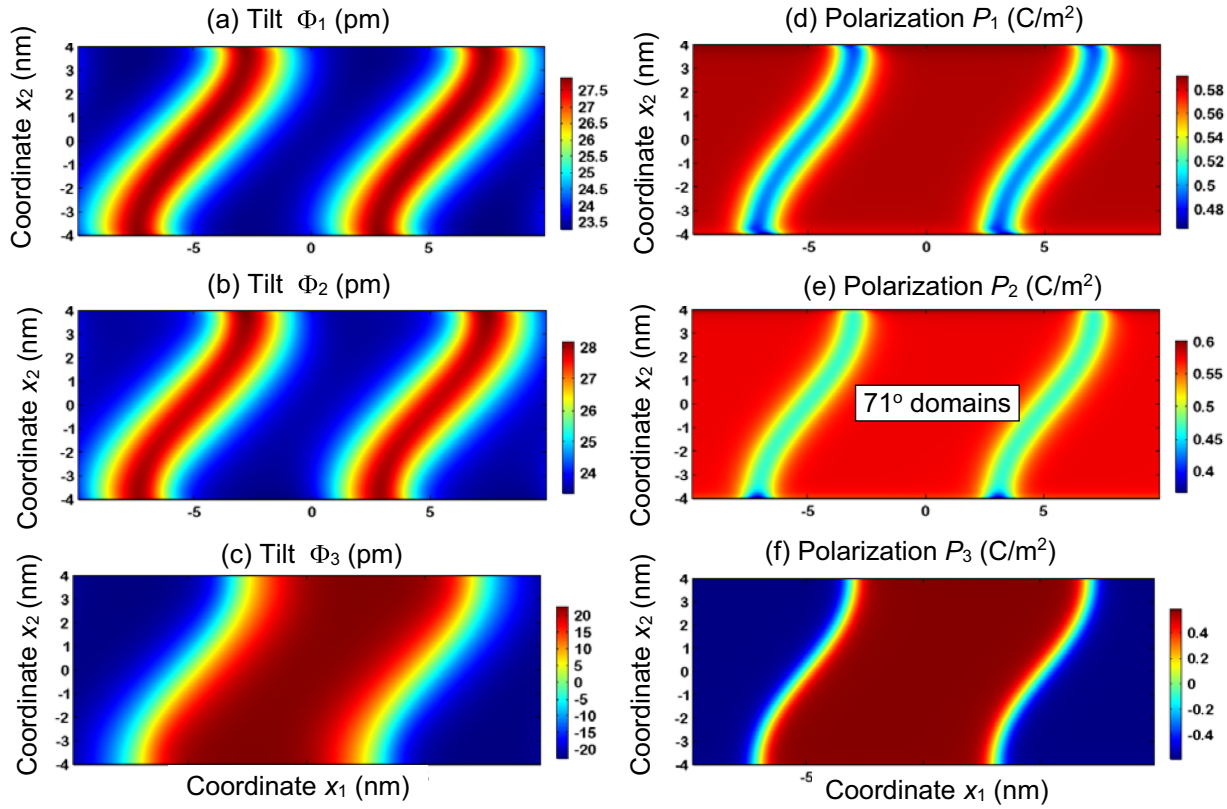

FIG. 8. {110} oriented 71° DWs in BFO film on $PrScO_3$ substrate (fully relaxed). Distribution of different components of the AFD order parameter Φ_i (a)–(c) and polarization P_i (d)–(f) in the $\{x_1x_2\}$ cross section of 7-nm BFO film with {110} oriented 71° DWs, room temperature.

and/or lattice strain (e.g., via electrostriction and flexoelectric coupling, $\delta u_{ij} \cong Q_{ijkl}P_kP_l + F_{ijkl}\frac{\partial P_k}{\partial x_l}$) can change the relative positions of the valence and conduction band via the deformation potential contribution, since $\partial E_{C,V}/\partial u_{ij} \sim \Xi_{ij}^{C,V}$ (deformation potential tensors are $\Xi_{ij}^{C,V}$). The change will be towards lower or higher band-gap conductivity dependently on the sign of the convolution, e.g., $\delta E_C(u_{ij}) \cong \Xi_{ij}^C \delta u_{ij}$ and/or $\delta E_V(u_{ij}) \cong \Xi_{ij}^V \delta u_{ij}$ (depending on the dominant contribution for *p*- or *n*-type doping). The trace of deformation potential tensor was estimated as $|\Xi_{ii}| \sim 20\,\text{eV}$ for *p*-doped BFO [44]. Since multiple experiments confirm the enhancement of the wall conductivity, we think that increased octahedral tilting (i.e., reduction of the Fe-O-Fe angle) should lead to a lower band gap. However, the inverse trend is not excluded for *n*-doped material.

Figure 9 shows the map of normalized static conductivity (that is directly proportional to CAFM contrast) across {101} oriented 180° DWs in 18-nm BFO film on PSO substrate. From the figure the DW can be one order of magnitude more conductive than the domain itself.

III. DISCUSSION

Based on the results above, we perform both experimental and theoretical investigations on the morphology and AFD-FE coupling at 180° and 71° domain walls. The comparison between the experimental and theoretical results gives more hints for AFD-FE coupling and corresponding functional manipulation.

Experimental results suggest that there are several kinks at the 180° domain walls, and corresponding polarization components also demonstrate some kinks. Despite the fact that the calculated AFD order parameters are larger than the experimental results, which may originate from the uncertain coefficients of coupling of strain with tilt and polarization, the AFD characteristics analyzed experimentally and theoretically share a lot of common features. The order parameter Φ_1 in Fig. 6(a) [corresponds to the oxygen displacements

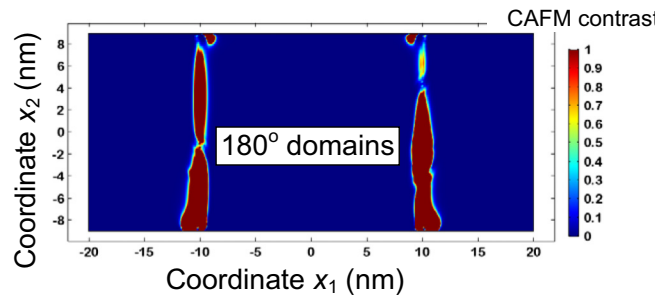

FIG. 9. Normalized static conductivity across {101} oriented 180° DWs in 18-nm BFO film on PSO substrate. Parameters are listed in Table I; the trace of deformation potential tensor is $\Xi_{ii}^C = 20\,\text{eV}$. Color bar is CAFM contrast in relative units.

analyzed in Fig. 2(e)] reveals two similar trianglelike regions with opposite displacements for each domain wall. More specifically, for the case of the upward polarization in the left and downward polarization in the right side of the wall, the oxygen columns would end up with a positive shift trianglelike region near the surface and a negative shift trianglelike region near the interface. For the case of the downward polarization in the left and upward polarization in the right side of the wall, the oxygen columns would end up with a negative shift trianglelike region near the surface and a positive shift trianglelike region near the interface. Note that the obvious decrease of oxygen tilt components near the interface observed experimentally is not corroborated by theoretical results for Φ_1 shown in Fig. 6(a). This may be related with different boundary conditions between experiments and calculations. The order parameter Φ_2 in Fig. 6(b) corresponds to the oxygen column displacements along the $[001]_{pc}$ direction in Fig. 2(f), where the inclination and meandering of AFD-FE walls are obvious. Moreover, theoretical results confirm that the values of the gradient energy coefficients for the oxygen tilt are critical to initiate the morphological changes of the 180° uncharged domain walls towards zigzag meandering. The meandering instability would appear at AFD-FE walls for small gradient energies, whereas the FE walls would become straighter and broaden at higher gradients (see Fig. S3 in the Supplemental Material [28]).

For 71° AFD-FE walls, the experimental and theoretical results are very close to each other, including the broader AFD walls compared with the FE walls, and the curvature of the AFD-FE walls at the interface and surface. The meandering instability and trianglelike regions appearing in the 180° AFD-FE walls are not observed in 71° AFD-FE walls. LGD theory proves that the width of the AFD wall increases with the tilt gradient coefficient, and the inclination of the 71° DW is determined by the conditions of electrical and mechanical compatibility, while the bending of the DW near the film surfaces is induced by the surface influence.

Based on the analyses above, we can conclude that the tilt gradient energy would greatly influence the AFD-FE coupling at the domain walls, and induce peculiar AFD-FE wall morphology according to different kinds of domain walls. Since the oxygen octahedra are reported to be strongly coupled with the electronic, magnetic, and optical properties [14,15], we assume that the different morphology induced by tilt gradient changes may correspond to the specific functionalities according to each DW.

In addition, we observed a significantly enhanced conductivity at the 180° AFD-FE walls. In accordance with theoretical estimates (see Fig. 9 and Appendix E in the Supplemental Material [28]), the conductivity enhancement at the domain wall can be caused by the electric potential changes and elastic strain variations inside the wall. The variations of the Fe-O-Fe bond angle, which uniquely determines the oxygen octahedral rotation, will result in the elastic strain changes via the rotostrictive effect. Further experimental investigations demonstrate an obvious decrease of Fe-O-Fe bond angles around the in-plane axis at these 180° domain walls, which is distinct from previous understanding that the reduced band gap is induced by strengthening the Fe-O-Fe bond angles around the z axis at 180° domain walls [16,17]. We propose that the reduction of the Fe-O-Fe bond angle can induce high conductivity at uncharged 180° domain walls.

IV. CONCLUSION

The coupling of AFD and FE long-range orders at the nominally uncharged 180° and 71° domain walls is investigated both experimentally and theoretically. Quite unexpectedly, 180° AFD-FE walls demonstrate rather unusual meandering characteristics and oxygen displacement trianglelike regions. However, in 71° domain walls, the AFD-FE coupling would result in broadened AFD walls and an obvious curvature near the interface and surface. LGD theory calculations agree with the experimental results very well and confirmed that the origin of the unusual AFD-FE walls is conditioned by the decrease of the tilt gradient energy in thin BFO films. For 180° AFD-FE walls, meandering instability appears for small gradient energies, while the walls become straighter and broaden at higher gradients [36]. However, uncharged 71° walls in thin films do not reveal any meandering instability, but their width increases with the tilt gradient coefficient increase. Moreover, we observe an obvious conduction at 180° AFD-FE walls accompanied by a decrease of Fe-O-Fe bond angles at 180° domain walls which are distinct from previous understanding that the reduced band gap is induced by strengthening Fe-O-Fe bond angles at 180° domain walls.

Based on this, we revealed experimentally and explained theoretically the previously unexplored type of the gradient-driven morphological phase transition taking place at the AFD-FE domain walls in thin strained multiferroic films. We also discover an unusual reduction of the *B*-O-*B* bond angle which can be responsible for the conduction at domain walls. These results help us better understand the AFD-FE coupling at domain walls and explore its possibility to induce physical properties for future nanodevices.

The data that support the findings of this study are available from the corresponding authors upon request.

ACKNOWLEDGMENTS

The authors express their sincere gratitude to the referee for useful remarks and stimulating discussions. This work is supported by the Key Research Program of Frontier Sciences CAS (QYZDJ-SSW-JSC010), the National Natural Science Foundation of China (Grants No. 51671194 and No. 51571197), and National Basic Research Program of China (2014CB921002). Y.L.T. acknowledges the IMR SYNL-T.S. Kê Research Fellowship and the Youth Innovation Promotion Association CAS (Grant No. 2016177). We are grateful to Mr. B. Wu and Mr. L. X. Yang of this lab for their technical support on the Titan platform of the G2 60–300 kV aberration-corrected scanning transmission electron microscope. A.N.M.'s work is partially supported by the National Academy of Sciences of Ukraine (Project No. 0117U002612) and has received funding from the European Union's Horizon 2020 research and innovation programme under the Marie Skłodowska-Curie Grant Agreement No. 778070. A portion of FEM was conducted

at the Center for Nanophase Materials Sciences, which is a DOE Office of Science User Facility (CNMS Proposal ID: 257).

M.J.H. and E.A.E. contributed equally to this work. X.L.M. and Y.L.Z. conceived the project of interfacial characterization in oxides by using aberration-corrected STEM. M.J.H., Y.L.Z., Y.L.T., and X.L.M. designed the experiments. M.J.H. performed the thin-film growth, STEM observations, and PFM/AFM measurement. Y.J.W. and X.W.G. carried out digital analysis of the STEM data. E.A.E. wrote the codes, performed numerical calculations, and prepared figures. A.N.M. generated the research idea, stated the problem, analyzed theoretical results, and wrote the theory part of the manuscript. All authors contributed to the discussions and manuscript preparation.

The authors declare no competing interests.

[1] Z. V. Gareeva, O. Diéguez, J. Íñiguez, and A. K. Zvezdin, Interplay between elasticity, ferroelectricity and magnetism at the domain walls of bismuth ferrite, Phys. Status Solidi RRL **10**, 209 (2016).

[2] J.-G. Park, M. D. Le, J. Jeong, and S. Lee, Structure and spin dynamics of multiferroic $BiFeO_3$, J. Phys.: Condens. Matter **26**, 433202 (2014).

[3] M. Fiebig, Revival of the magnetoelectric effect, J. Phys. D: Appl. Phys. **38**, R123 (2005).

[4] J. Seidel, L. W. Martin, Q. He, Q. Zhan, Y-H. Chu, A. Rother, M. E. Hawkridge, P. Maksymovych, P. Yu, M. Gajek, N. Balke, S. V. Kalinin, S. Gemming, F. Wang, G. Catalan, J. F. Scott, N. A. Spaldin, J. Orenstein, and R. Ramesh, Conduction at domain walls in oxide multiferroics, Nat. Mater. **8**, 229 (2009).

[5] Z. Chen, J. Liu, Y. Qi, D. Chen, S.-L. Hsu, A. R. Damodaran, X. He, A. T. N'Diaye, A. Rockett, and L. W. Martin, 180 degrees ferroelectric stripe nanodomains in $BiFeO_3$ thin films, Nano Lett. **15**, 6506 (2015).

[6] W. Geng, X. Guo, Y. Zhu, Y. Tang, Y. Feng, M. Zou, Y. Wang, M. Han, J. Ma, B. Wu, W. Hu, and X. Ma, Rhombohedral–orthorhombic ferroelectric morphotropic phase boundary associated with a polar vortex in $BiFeO_3$ films, ACS Nano **12**, 11098 (2018).

[7] S. Y. Yang, J. Seidel, S. J. Byrnes, P. Shafer, C.-H. Yang, M. D. Rossell, P. Yu, Y.-H. Chu, J. F. Scott, J. W. Ager III, L. W. Martin, and R. Ramesh, Above-bandgap voltages from ferroelectric photovoltaic devices, Nat. Nanotechnol. **5**, 143 (2010).

[8] C. Paillard, X. Bai, I. C. Infante, M. Guennou, G. Geneste, M. Alexe, J. Kreisel, and B. Dkhil, Photovoltaics with ferroelectrics: Current status and beyond, Adv. Mater. **28**, 5153 (2016).

[9] G. Catalan, J. Seidel, R. Ramesh, and J. F. Scott, Domain wall nanoelectronics, Rev. Mod. Phys. **84**, 119 (2012).

[10] M. Daraktchiev, G. Catalan, and J. F. Scott, Landau theory of domain wall magnetoelectricity, Phys. Rev. B **81**, 224118 (2010).

[11] A. Aird and E. K. H. Salje, Sheet superconductivity in twin walls: Experimental evidence of WO_{3-x}, J. Phys.: Condens. Matter **10**, L377 (1998).

[12] Z. Gareeva, O. Diéguez, J. Íñiguez, and A. K. Zvezdin, Complex domain walls in $BiFeO_3$, Phys. Rev. B **91**, 060404(R) (2015).

[13] E. A. Eliseev, A. N. Morozovska, Y. Gu, A. Y. Borisevich, L.-Q. Chen, V. Gopalan, and S. V. Kalinin, Conductivity of twin-domain-wall/surface junctions in ferroelastics: Interplay of deformation potential, octahedral rotations, improper ferroelectricity, and flexoelectric coupling, Phys. Rev. B **86**, 085416 (2012).

[14] J. M. Rondinelli, S. J. May, and J. W. Freeland, Control of octahedral connectivity in perovskite oxide heterostructures: An emerging route to multifunctional materials discovery, MRS Bull. **37**, 261 (2012).

[15] F. Xue, Y. Gu, L. Liang, Y. Wang, and L. Q. Chen, Orientations of low-energy domain walls in perovskites with oxygen octahedral tilts, Phys. Rev. B **90**, 220101(R) (2014).

[16] G. Catalan and J. F. Scott, Physics and applications of bismuth ferrite, Adv. Mater. **21**, 2463 (2009).

[17] G. Catalan, On the link beween octahedral rotations and conductivity in the domain walls of $BiFeO_3$, Ferroelectrics **433**, 65 (2012).

[18] A. Lubk, S. Gemming, and N. A. Spaldin, First-principles study of ferroelectric domain walls in multiferroic bismuth ferrite, Phys. Rev. B **80**, 104110 (2009).

[19] A. Y. Borisevich, E. A. Eliseev, A. N. Morozovska, C.-J. Cheng, J.-Y. Lin, Y. H. Chu, D. Kan, I. Takeuchi, V. Nagarajan, and S. V. Kalinin, Atomic-scale evolution of modulated phases at the ferroelectric-antiferroelectric morphotropic phase boundary controlled by flexoelectric interaction, Nat. Commun. **3**, 775 (2012).

[20] Y. L. Tang, Y. L. Zhu, Y. Liu, Y. J. Wang, and X. L. Ma, Giant linear strain gradient with extremely low elastic energy in a perovskite nanostructure array, Nat. Commun. **8**, 15994 (2017).

[21] A. N. Morozovska, E. A. Eliseev, M. D. Glinchuk, L. Q. Chen, and V. Gopalan, Interfacial polarization and pyroelectricity in antiferrodistortive structures induced by a flexoelectric effect and rotostriction, Phys. Rev. B **85**, 094107 (2012).

[22] E. A. Eliseev, S. V. Kalinin, Y. Gu, M. D. Glinchuk, V. Khist, A. Borisevich, V. Gopalan, L.-Q. Chen, and A. N. Morozovska, Universal emergence of spatially modulated structures induced by flexoantiferrodistortive coupling in multiferroics, Phys. Rev. B **88**, 224105 (2013).

[23] J. Wang, J. B. Neaton, H. Zheng, V. Nagarajan, S. B. Ogale, B. Liu, D. Viehland, V. Vaithyanathan, D. G. Schlom, U. V. Waghmare, N. A. Spaldin, K. M. Rabe, M. Wuttig, and R. Ramesh, Epitaxial $BiFeO_3$ multiferroic thin film heterostructures, Science **299**, 1719 (2003).

[24] A. Y. Borisevich, O. S. Ovchinnikov, H. Jung Chang, M. P. Oxley, P. Yu, J. Seidel, E. A. Eliseev, A. N. Morozovska, R. Ramesh, S. J. Pennycook, and S. V. Kalinin, Mapping octahedral tilts and polarization across a domain wall in $BiFeO_3$ from Z-contrast scanning transmission electron microscopy image atomic column shape analysis, ACS Nano, **4**, 6071 (2010).

[25] S. M. Anthony and S. Granick, Image analysis with rapid and accurate two-dimensional Gaussian fitting, Langmuir **25**, 8152 (2009).

[26] Y. L. Tang, Y. L. Zhu, X. L. Ma, A. Y. Borisevich, A. N. Morozovska, E. A. Eliseev, W. Y. Wang, Y. J. Wang, Y. B. Xu,

Z. D. Zhang, and S. J. Pennycook, Observation of a periodic array of flux-closure quadrants in strained ferroelectric $PbTiO_3$ films, Science **348**, 547 (2015).

[27] Y. Liu, Y.-L. Zhu, Y.-L. Tang, Y.-J. Wang, Y.-X. Jiang, Y.-B. Xu, B. Zhang, and X. Ma, Local enhancement of polarization at $PbTiO_3/BiFeO_3$ interfaces mediated by charge transfer, Nano Lett. **17**, 3619 (2017).

[28] See Supplemental Material at http://link.aps.org/supplemental/10.1103/PhysRevB.100.104109 for calculation details placed in Appendixes A–E.

[29] Y. Gu, K. Rabe, E. Bousquet, V. Gopalan, and L. Q. Chen, Phenomenological thermodynamic potential for $CaTiO_3$ single crystals, Phys. Rev. B **85**, 064117 (2012).

[30] J. H. Barrett, Dielectric constant in perovskite type crystals, Phys. Rev. **86**, 118 (1952).

[31] A. K. Tagantsev, J. Fousek, and L. E. Cross, *Domains in Ferroic Crystals and Thin Films* (Springer, New York, 2010).

[32] L. D. Landau, L. P. Pitaevskii, M. Kosevich, and E. M. Lifshitz, *Theory of Elasticity*, Theoretical Physics Vol. 7 (Butterworth-Heinemann, Oxford, 1976).

[33] D. V. Karpinsky, E. A. Eliseev, F. Xue, M. V. Silibin, A. Franz, M. D. Glinchuk, I. O. Troyanchuk, S. A. Gavrilov, V. Gopalan, L.-Q. Chen, and A. N. Morozovska, Thermodynamic potential and phase diagram for multiferroic bismuth ferrite ($BiFeO_3$), npj Comput. Mater. **3**, 20 (2017).

[34] Supplemental Material of A. N. Morozovska, E. A. Eliseev, M. D. Glinchuk, O. M. Fesenko, V. V. Shvartsman, V. Gopalan, M. V. Silibin, and D. V. Karpinsky, Rotomagnetic coupling in fine-grained multiferroic $BiFeO_3$: Theory and experiment, Phys. Rev. B **97**, 134115 (2018).

[35] J. X. Zhang, Y. L. Li, Y. Wang, Z. K. Liu, L. Q. Chen, Y. H. Chu, F. Zavaliche, and R. Ramesh, Effect of substrate-induced strains on the spontaneous polarization of epitaxial $BiFeO_3$ thin films, J. Appl. Phys. **101**, 114105 (2007).

[36] E. A. Eliseev, A. N. Morozovska, C. T. Nelson, and S. V. Kalinin, Intrinsic structural instabilities of domain walls driven by gradient coupling: Meandering antiferrodistortive-ferroelectric domain walls in $BiFeO_3$, Phys. Rev. B **99**, 014112 (2019).

[37] A. K. Tagantsev, E. Courtens, and L. Arzel, Prediction of a low-temperature ferroelectric instability in antiphase domain boundaries of strontium titanate, Phys. Rev. B **64**, 224107 (2001).

[38] P. V. Yudin, R. Ahluwalia, and A. K. Tagantsev, Upper bounds for flexocoupling coefficients in ferroelectrics, Appl. Phys. Lett. **104**, 082913 (2014).

[39] N. A. Pertsev, A. G. Zembilgotov, and A. K. Tagantsev, Effect of Mechanical Boundary Conditions on Phase Diagrams of Epitaxial Ferroelectric Thin Films, Phys. Rev. Lett. **80**, 1988 (1998).

[40] T. M. Gesing, R. Uecker, and J. C. Buhl, Refinement of the crystal structure of praseodymium orthoscandate, $PrScO_3$, Z. Kristallogr. - New Cryst. Struct. **224**, 365 (2009).

[41] E. A. Eliseev, A. N. Morozovska, G. S. Svechnikov, P. Maksymovych, and S. V. Kalinin, Domain wall conduction in multiaxial ferroelectrics: Impact of the wall tilt, curvature, flexoelectric coupling, electrostriction, proximity and finite size effects, Phys. Rev. B **85**, 045312 (2012).

[42] E. A. Eliseev, Y. M. Fomichov, S. V. Kalinin, Y. M. Vysochanskii, P. Maksymovich, and A. N. Morozovska, Labyrinthine domains in ferroelectric nanoparticles: Manifestation of a gradient-induced morphological phase transition, Phys. Rev. B **98**, 054101 (2018).

[43] A. N. Morozovska, R. K. Vasudevan, P. Maksymovych, S. V. Kalinin, and E. A. Eliseev, Anisotropic conductivity of uncharged domain walls in $BiFeO_3$, Phys. Rev. B **86**, 085315 (2012).

[44] Z. Fu, Z. G. Yin, N. F. Chen, X. W. Zhang, H. Zhang, Y. M. Bai, and J. L. Wu, Biaxial stress-induced giant bandgap shift in $BiFeO_3$ epitaxial films, Phys. Status Solidi RRL **6**, 37 (2012).